THE JOURNAL OF PHYSICAL CHEMISTRY C
A JOURNAL OF THE AMERICAN CHEMICAL SOCIETY

pubs.acs.org/JPCC
Article

Comparison of Industrially Relevant Fischer–Tropsch Cobalt Catalysts Supported on Alumina and Modified Silica with Complementary *In-Situ* and *Operando* Characterization Methods

Anna Zimina,* Mohamed I. Fadlalla, Jana Potgieter,* Catalina E. Jimenez,* Rabia Ilica, Enrico Sireci, Dmitry I. Sharapa, Dominic de Oliveira, Cherie Hsu, Erisa Saraci, Moritz Wolf, Pinar Sakoglu, Athanasios Skaltsogiannis, Tianli Zhong, Marcus Bär, Thys Botha, Denzil Moodley, Michael Claeys,* Felix Studt, and Jan-Dierk Grunwaldt

Cite This: https://doi.org/10.1021/acs.jpcc.5c05172

Read Online

ACCESS | Metrics & More | Article Recommendations | Supporting Information

ABSTRACT: Power-to-liquid processes are considered a crucial route to substitute petroleum-based processes for the production of valuable chemicals and liquid fuels, opening the possibility for the production of sustainable aviation fuels. Two selected catalysts, 20wt.%Co/Al_2O_3 (CA) and 20wt.%Co/TiO_2–SiO_2 (CTS), were tested in the Fischer–Tropsch synthesis (FTS) reaction under industrially relevant conditions. The CTS catalyst showed 10% higher activity, improved C_{5+} selectivity, and lower methane formation than the CA catalyst. The components of these complex catalysts were characterized, and the structural evolution of cobalt during activation and reaction was monitored by various *in-situ* and *operando* methods. H_2 temperature-programmed reduction, X-ray diffraction, magnetometry, and X-ray absorption spectroscopy revealed a decrease in the temperature of stepwise cobalt reduction in CTS catalysts compared to CA. The reduction behavior of Co during activation was dependent on the support nature and strength of the metal–support interaction. The formation of composites with the support was proposed based on the results obtained by bulk probing XAS and more surface-sensitive NEXAFS methods. XRD, magnetometry, and XAS revealed that the size of the activated Co particles was dependent on the support chosen. The DFT modeling results confirmed the higher affinity of cobalt for titania, which might explain the smaller Co crystallite size and higher stability observed for the CTS catalyst. The difference in activity between the two commercially relevant cobalt-based catalysts on different supports could be linked to the difference in pore sizes and the strength of the metal–support interaction.

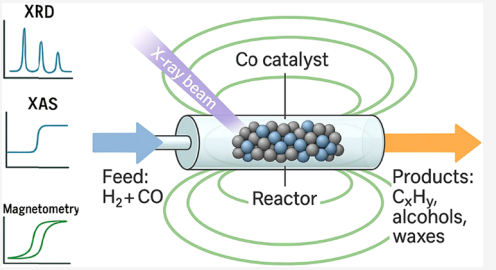

INTRODUCTION

Power-to-liquid (PtL) processes are considered as a crucial route to substitute petroleum-based processes for the production of valuable chemicals and liquid fuels,[1−3] opening the possibility for the production of sustainable aviation fuels (SAF).[4−7] Syngas, a mixture of H_2 and CO, obtained from renewable sources like water electrolysis, carbon capture processes, or local CO_2-emission sources, can be converted via Fischer–Tropsch synthesis (FTS) into long-chain hydrocarbons. In commercial applications, cobalt-based catalysts, using high surface area materials like γ-Al_2O_3,[6] TiO_2,[8,9] or SiO_2[10,11] are widely applied in order to obtain well-dispersed metal particles and to prevent their sintering.[12,13] In addition, modifiers like Ti or Zr on SiO_2 and Si/La/B on γ-Al_2O_3 are used.[14] From an economic point of view, high catalytic activity, stability, and selectivity to C_{5+} products, as well as low selectivity to byproducts like CH_4, are desirable.[15,16] Product selectivity can be tuned by the operating conditions (temperature, pressure, syngas composition) or the catalyst composition.[15] In particular, the atomic structure of the active particles, morphology, and porosity of support grains, as well as the strength of metal–support interaction, are decisive.[14] The interaction between the active Co nanoparticles and the support is crucial, as weak metal–support interactions (MSI) lead to stronger sintering,[17] and strong MSI may hamper the reducibility of the parent cobalt catalyst due to the formation of $CoAl_2O_4$, $CoTiO_3$, or Co_2SiO_4. In addition, the formation of these metal–support compounds (MSCs) during FTS is known to cause deactivation.[18−20]

Fischer–Tropsch synthesis (FTS) requires a thoughtful catalyst design to improve performance, selectivity, and stability by tuning the strength of the metal–support interaction, the cobalt nanoparticle size, and the presence of

Received: July 25, 2025
Revised: January 23, 2026
Accepted: January 30, 2026

specific cobalt phases formed during the reaction under industrially relevant conditions.[20−27] Such optimization has often been approached by investigating the role of individual aspects relevant to the performance of technical catalysts with industrial complexity. In most cases, one parameter, like nanoparticle size,[28−30] support,[17,31−33] or reduction promoters,[34] has been varied. It is known that Co particles smaller than 8 nm favor methane formation,[35] are more prone to oxidation,[36,37] are more difficult to reduce, and subsequently require reduction promoters for milder reduction.[14] In addition, there are very few studies that focus on the direct comparison of different supports. Storsaeter et al.[33] reported that the reduction of γ-Al_2O_3 and SiO_2 depended on the pore size, whereas sintering was observed in TiO_2. A two-step reduction process involving Co_3O_4 to CoO and CoO to Co^0 transformation revealed both weak interactions (e.g., Co/SiO_2) and strong interactions (e.g., Co/Al_2O_3) with the support.[34] Promotion with ZrO_2 or TiO_2 on γ-Al_2O_3 and SiO_2 has been reported to improve the surface structures.[38] Additionally, often noble metals like platinum are added as reduction promoters in cobalt-based Fischer−Tropsch (FT) catalysts.[39]

Industrial catalysts are not only dynamic but also have a complex pore structure and grain morphology that influence the cobalt particle size and strength of the MSI and often contain a reduction promoter. A complementary pool of techniques that allows insight under *in-situ* and *operando* conditions is required. To show this endeavor, two catalysts with significantly different catalytic activities were selected: (1) a 20wt.%Co/Al_2O_3 catalyst (CA) with a microporous support structure and good catalytic performance, and (2) a 20wt.% Co/SiO_2, where the support has been coated with titania (CTS), which shows enhanced catalytic activity and lower methane selectivity.

In this study, we compared these two commercially relevant FT catalysts by using different complexity scales and complementary advanced characterization methods. The selected analysis tools are particularly designed to investigate the active phases under industrially relevant reaction conditions. Hence, the proposed approach bridges the gap between industry and academia and documents the future potential of *in-situ* and *operando* characterization of catalysts for developing a deeper understanding with respect to the metal−support interactions, long-term stability, and deactivation phenomena to improve commercially relevant catalysts in the overall FT process to efficiently produce SAF.

METHODS

For the alumina-supported system (CA): 20 wt.% Co supported on Sasol Germany's Puralox SCCa γ-Al_2O_3 catalyst was prepared by SASOL S.A. on a laboratory scale, as described elsewhere.[40] More precisely, 20 wt.% Co was deposited on the alumina support via a slurry-phase impregnation procedure with aqueous metal precursor solutions. The resulting slurry was dried under vacuum and calcined in static air at 250 °C. Sequential impregnation and calcination steps were applied to achieve a 20 wt.% Co nominal loading. For the silica-supported system (CTS), specific support modifications were done: an appropriate amount of Ti-isopropoxide was added to anhydrous EtOH in a round-bottom flask. Thereafter, the silica gel support was added to the latter, and the sample was dried under reduced pressure to obtain a free-flowing powder.[41] The material was calcined in a muffle oven in air at 500 °C for 2 h to provide a titania-modified silica support. A 20wt.%Co/Ti-SiO_2 catalyst was prepared by two-step slurry impregnation of the modified support with aqueous cobalt nitrate solution, followed by the appropriate drying and calcination steps, as described previously.[42]

The surface areas of the samples were determined by N_2-physisorption at −196 °C with a BELSORP-mini II (Rubotherm) and calculated using the Brunauer−Emmett−Teller (BET) method in the p/p_0 = 0.05−0.30 range (16 data points) (Belsorp Adsorptions/Desorptions Data Analysis Software). Before each measurement, ca. 150 mg of the sample was heated for 2 h at 300 °C in a vacuum for drying.

The cobalt phases in the calcined state were characterized via XRD on a Bruker D8 Advance diffractometer. Measurements were performed with a Co K_α source (Co $K_{\alpha1}$ = 1.79026 Å; Co $K_{\alpha2}$ = 1.792850 Å) between 5° and 129°, with an increment of 0.024° and a measuring time of 2 h. The diffraction patterns were analyzed with the X'Pert HighScore software, and Topas 5.0[43] was used for the Rietveld refinements[44] using the fundamental parameter approach. The full pattern refinement technique was used to determine the average crystallite size.

Temperature-programmed reduction (TPR) profiles of the catalysts were recorded on an Autochem 2910 (Micromeritics Co., USA) instrument. Approximately 50 mg of the sample was placed in a U-shaped quartz tube fitted with a thermocouple for continuous temperature measurements. The sample was dried under helium flow (50 mL/min) by increasing the temperature from room temperature at 5 °C/min to 120 °C, where it was held constant for 10 min to remove water. The sample was then cooled to room temperature, subsequently heated to 900 °C at 10 °C/min in a flow (50 mL/min) of 10%H_2/Ar and kept at this temperature for 10 min. The water formed during the reduction was trapped using a dry ice/acetone bath. The amount of hydrogen consumed during reduction was measured with a thermal conductivity detector (TCD).

FTS test runs at SASOL laboratory were performed in a slurry phase in a continuously stirred tank reactor (CSTR) with a reactor volume of 1000 mL. Catalyst samples (10−15 g) were prereduced at 425 °C under atmospheric pressure, as described in a recently published patent.[45] The sample was suspended in molten hydrogenated wax inside the reactor. Realistic FTS conditions were used (230 °C, 19 bar), and the synthesis gas conversion was kept constant in each run by adjusting the GHSV. The synthesis gas flow was regulated using Brooks mass flow controllers. As the CA catalyst is prone to deactivation at higher water partial pressures, as demonstrated earlier,[41] it was run at lower conversion levels than the CTS catalyst. A direct comparison of selectivity, thus, cannot be done at iso-conversion levels.

The effect of the catalyst support on the Co_3O_4 nanoparticle reduction pathway of the nanoparticles deposited on the supports in an H_2 environment was examined using an *in-situ* XRD reaction cell.[46,47] The sample (ca. 0.18 mg) was packed in a capillary cell (quartz, OD 1.0 mm) and heated with an infrared heater. *In-situ* XRD analysis was conducted using a Bruker D8 Advance diffractometer equipped with a VANTEC position-sensitive detector and Mo source ($K_{\alpha1}$ = 0.709 Å). Scans were obtained at 5 min intervals in the temperature ranges of 50 to 420 °C and 370 °C (and held for 6 h) for the CA and CTS catalysts, respectively, with a heating rate of 1 °C/min (a scan every 5 °C). Each scan was obtained with a step size of 0.018°, time/step of 0.2 s, and total scan time of 4 min. Rietveld refinement analysis[44] was conducted using the TOPAS 5.0 software package[43] to determine the phase composition and crystallite size as a function of the reduction temperature.

An *in-situ* magnetometer[37,48,49] (developed in collaboration between UCT and SASOL) with a magnetic field strength of 2 T (20 kOe) was utilized. The catalyst (150 mg) was diluted with 1000 mg of SiC and placed in the isothermal zone of the reactor; the temperature was monitored with an N-type thermocouple positioned in the catalyst bed. The temperature of the catalyst bed was increased from 50 to 420 °C and 370 °C (and held for 6 h) for the CA and CTS catalysts, respectively, at a heating rate of 1 °C/min under a H_2 flow of 8.5 mL/min. Magnetic saturation (M_{sat}) measurements were performed every 5 min. The degree of reduction (DoR) of Co_3O_4 to $Co^0$is obtained using eq 1

https://doi.org/10.1021/acs.jpcc.5c05172
J. Phys. Chem. C XXXX, XXX, XXX−XXX

$$\mathrm{DoR}(\%) = \frac{M_{\mathrm{sample}} \cdot 0.15\ \mathrm{g}}{M_{\mathrm{calibration}} \cdot X_{\mathrm{loading}} \cdot m_{\mathrm{unreducedsample}}} \cdot 100 \quad (1)$$

where M_{sample} and $M_{\mathrm{calibration}}$ are the magnetizations of the sample and of the cobalt calibration sample (1 g) (in emu), respectively. X_{loading} is the ICP-OES determined cobalt metal loading, and $m_{\mathrm{unreducedsample}}$ is the mass of the unreduced sample loaded into the reactor. During the *in-situ* magnetometer reduction, γ was recorded to determine changes in the superparamagnetic fraction of the metallic Co nanoparticle size distribution[22] using eq 2

$$\gamma(T) = \frac{2 \cdot M_{\mathrm{rem}}(T)}{M_{\mathrm{sat}}(T)} \cdot 100\ \mathrm{wt\%} \quad (2)$$

where M_{rem} is the remnant magnetization (measured at 0 T), and M_{sat} is the saturation magnetization (measured at 2 T). An increase in the γ values can be interpreted as an indication that sintering is occurring.

Sizing experiments were carried out by using *in-situ* magnetometry. Following the reduction, a 32 min magnetization vs field strength measurement (M−H measurement) was conducted, varying the field strength from 2T to −2T and back to 2T. This data was used for magnetometry-based sizing by applying a linear combination fit of the Langevin equation[50,51] (eq 3) as a function of particle size to obtain a size distribution that fits the experimental data. The Langevin equation is applicable only to superparamagnetic materials, which display zero remanent magnetization. Previous work has shown that the Langevin equation remains applicable for γ < 10% without significant errors.[29,50,52]

$$\frac{M}{M_s} = \coth\left(\frac{\rho \pi \sigma_s d^3 H}{6 k_B T}\right) - \frac{6 k_B T}{\rho \pi \sigma_s d^3 H} \quad (3)$$

where M_s is the saturation magnetization, ρ is the density, σ_s is the mass-specific saturation magnetization of the bulk material, H is the field strength, d is the particle diameter, k_B is the Boltzmann constant, and T is the temperature.

Above a certain critical size, these particles display nonsuperparamagnetic behavior, where they exhibit remanent magnetization. The percentage of particles greater than this critical size can be estimated using γ (eq 2). The critical size is also known to be dependent on temperature, where $\mathrm{Dc} \propto T^{1/3}$.[53] To apply the Langevin equation to samples that do not display superparamagnetism, we propose to utilize the temperature dependence of the critical diameter by conducting measurements at higher temperatures to decrease the remanent magnetization. In these experiments, the measurement temperature was increased from the reduction temperature of 370 °C to 400 °C, 500 °C, and 600 °C, with M−H measurements being conducted before ramping to temperature, at the temperature, and after the temperature ramp to perform the sizing experiments and to confirm that no changes in the size of the material were observed.

For the fit of the Langevin equation, an increment size of 0.05 nm was used to generate the required theoretical curves. The best fit of a linear combination of these curves was then identified using two methods: first, by RSS optimization using a sequential quadratic programming algorithm,[54,55] and second, by fitting a log-normal distribution by optimizing μ and σ parameters of the log-normal distribution function (eq 4).

$$f(x) = \frac{1}{x\sigma\sqrt{2\pi}} \exp\left(-\frac{(\ln x - \mu)^2}{2\sigma^2}\right),\ x > 0 \quad (4)$$

FTS test runs at University of Cape Town laboratory were performed in a similar type of reactor as at the SASOL site for 3 h (10 mg of catalysts, p = 19 bar, T = 230 °C, H_2/CO = 2.0) and under the same constrains.[41]

X-ray absorption (XAS) measurements at the Co K-edge (7709 eV) were carried out at the CAT-ACT beamline[56] of the KIT Light Source[57] in transmission mode using high-energy ionization chambers (Ohyo Koken Kogyo Co. Ltd., Japan). The energy of the X-ray photons was selected by a double-crystal monochromator with Si(111) crystal pairs. The beam size for the measurements was set with slits to 1.0 × 2.0 (horizontal × vertical) mm^2. Data reduction and extraction of the μ(k) function (with a Rbkg value of 1) were performed using the Athena code, and EXAFS data were fitted with the corresponding crystalline phases using the Artemis package of IFFIT Software (version 0.9.26).[58] Linear combination analysis (LCA) was performed using the reference spectra measured on Co foil, CoO and Co_3O_4 powders in pellet form. *Operando* XAS measurements were performed in a continuous flow high-pressure reactor developed at KIT.[59] A fixed-bed reactor with an inner volume of about 0.1 mL was used for *in-situ* temperature-programmed reduction (TPR) and *operando* FTS. 10 mL/min pure hydrogen was used as a reducing agent during TPR. The temperature was increased with a ramp of 1°C/min from room temperature to 370−450 °C. FTS catalysts were diluted with the corresponding support material at a ratio of 1:6. The reaction conditions are P = 20−25 bar, T = 200−250 °C, and H_2:CO = 2.0. The gas phase was analyzed using an online μGC (Inficon GmbH, Germany).

The reducibility of cobalt in the CA and CTS catalysts near the solid/gas interface was compared by using *in-situ* near-edge X-ray fine-structure (NEXAFS) at the Co L_3-edge (778 eV) in the near-ambient pressure high-energy X-ray photoelectron spectroscopy (NAP-HE-XPS) endstation, developed by the FHI/MPI-CEC for the ISISS beamline located at the BESSY II light source operated by the Helmholtz-Zentrum Berlin für Materialien und Energie GmbH (HZB).[60] For this, 0.5 g of CA and CTS catalysts were prereduced at 1 bar under 20 mL/min of pure H_2 flow, heating at 2.5 K/min from 25 °C up to 380 °C, holding for 3 h, and cooling fast back to 25 °C. The purpose of this treatment is to preserve the achieved degree of reduction for the CA and CTS catalysts, which requires a pure H_2 flow at 1 bar, as in the other methods. After cooling, the samples were purged with Ar and then transferred to an Ar glovebox to be pelletized, mounted on sapphire sample holders, and brought to ISISS inside an Ar transfer box. *In-situ* NEXAFS was carried out in total electron yield (TEY) mode, illuminating a 100 × 80 μm^2 spot (horizontal × vertical) on the pellet under 0.25 mbar H_2 during heating CTS up to 325 °C and CA up to 375 °C. Linear combination analysis of the Co L_3-edge NEXAFS spectra was performed using the Athena program (Demeter version 0.9.26),[58] using divalent CoO and Co(0001) single crystals as reference materials. Further details are provided in the SI, Figure S1. Au 4f was measured on a gold foil with a photon energy of 774 eV, i.e., in the pre-edge region of the Co L-edge, for energy calibration. The energy resolution was about 0.15 eV.

Spin-polarized DFT calculations were performed using the software VASP version 6.2[61,62] with the GGA functional BEEF-vdW[63] and the projector-augmented wave (PAW) method with standard PAW potentials.[64] Gaussian smearing with a width of 0.1 eV was used in all calculations, and the sampling of the Brillouin zone was carried out in a Monkhorst−Pack grid with a k-point linear spacing of approximately 1.78 Å^{-1}, that is, a (14 × 14 × 1) grid for the (1 × 1) fcc-Co (111) surface. Bulk calculations were carried out with an energy cutoff of 600 eV, which was changed to 400 eV for all other calculations. The convergence of the SCF cycle was set at an energy difference of 10^{-6} eV, while ionic convergence was achieved when the atomic forces were below 0.01 eV/ Å. A vacuum of at least 15 Å was used in all of the calculations. In order to mimic the interactions between Co and the different supports, we calculated the adhesion energies (Y_{adh}) between the metal and the support slabs. The (111) surface of fcc-Co was chosen for the interface models, as this is the most stable facet[65,66] and thus more likely to be found at the interface. The employed procedure was similar to the one described in a previous work by our group.[67]

RESULTS

In this study, a commercial benchmark 20wt.%Co/alumina catalyst (CA) and a newly developed commercially relevant 20wt.%Co/modified silica catalyst (CTS) are compared. The CTS catalyst was ca. 10% more active during FTS than the benchmark CA catalyst, with a significant shift in selectivity

https://doi.org/10.1021/acs.jpcc.5c05172
J. Phys. Chem. C XXXX, XXX, XXX−XXX

toward higher hydrocarbons, as shown in Figure 1. The C_{5+} selectivity of the CTS catalyst was 3−5% higher than that of

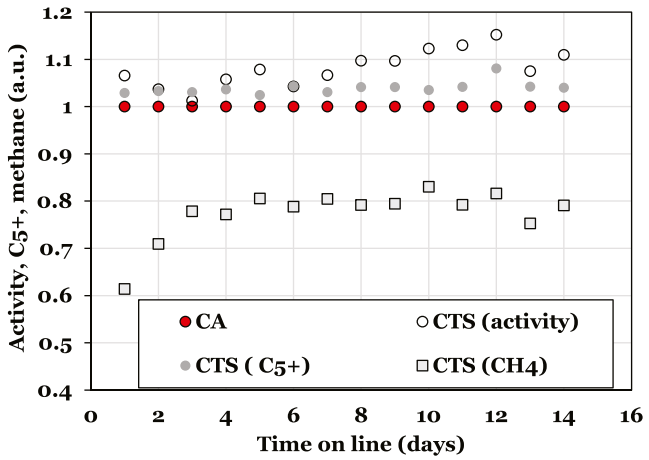

Figure 1. Comparison of the catalytic activity from slurry phase testing for the two selected CA and CTS catalysts conducted over 2 weeks (230 °C, 19 bar, reactor H_2:CO = 2.0) with relative catalytic activity (circles), C_{5+} selectivity (open circles), and methane selectivity (open squares).

the CA catalyst, while the methane selectivity was about 20% lower (see open circles and squares in Figure 1, respectively). Toward the end of the runs, there were some changes in the H_2/CO inlet ratio (the syngas supply was from an autothermal reformer), which caused some natural fluctuations in the data unrelated to catalyst deactivation. The difference in the catalytic performance of the CA and CTS catalysts may be linked to the difference in their atomic structure, in the chemical state of the active phases, or in the morphology/structural properties of the support, i.e., the porosity, the shape, and the surface roughness of support grains. To understand the structure−performance (selectivity/activity) relationship for these two selected systems, a number of complementary characterization methods were applied.

The textural properties of both supports and the resulting CA and CTS catalysts, as determined by N_2 physisorption, are shown in Table 1. The alumina support has a higher surface

Table 1. Specific Surface Areas (S_{BET}), Average Pore Diameters (d_{pav}), and Pore Volumes (V_p) of the Supports and Calcined Catalysts

samples	S_{BET}, m^2/g	d_{pav}, nm	V_p, cm^3/g
Support CA	136.5	12.7	0.44
Catalyst CA	95.0	10.6	0.25
Support CTS	91.2	30.2	0.69
Catalyst CTS	65.9	25.6	0.42

area and a smaller average pore size compared with the silica support. The specific surface area decreased by about 30% in both cases when 20% cobalt was deposited by slurry phase impregnation, indicating that cobalt oxide occupied some of the pore volume. Nevertheless, the size of the mesopores hardly changed after Co impregnation.

XRD measurements confirmed that the support for the CA catalyst remained in a crystalline phase of a mixture of γ- and α-alumina,[68] whereas the support for the CTS catalyst contained an amorphous silica (Figure 2). The reflection

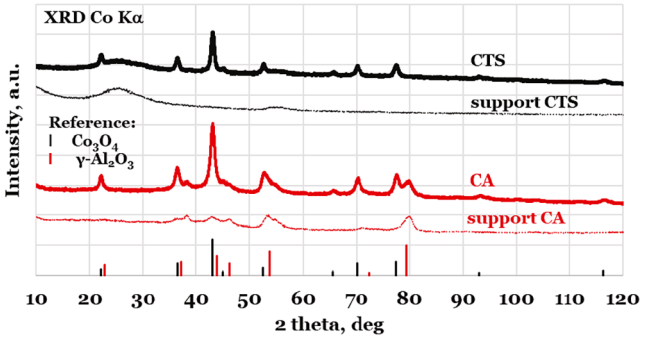

Figure 2. XRD patterns of the pure alumina (red dotted line) and silica (black dotted line) supports and the corresponding calcined CA and CTS catalysts (solid lines).

pattern corresponding to the spinel Co_3O_4 was observed in both calcined samples, and no additional crystalline cobalt phase was present. The average crystallite size of the Co_3O_4 particles was estimated by Rietveld refinement. The cobalt oxide particles were larger (about 30%) in the calcined CTS catalyst (20 nm) than in the CA catalyst (15 nm).

Figure 3 shows the H_2−temperature-programmed reduction (TPR) profiles of the two catalysts. It is well-known that the

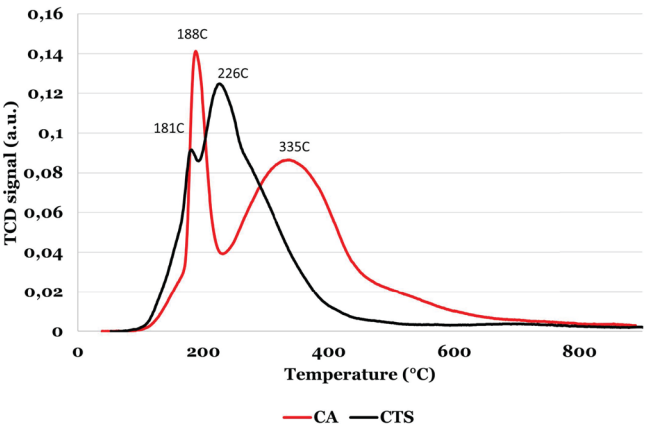

Figure 3. H_2-TPR profiles of the calcined CA (red line) and CTS (black line) catalysts (temperature ramp rate of 10 °C/min in 10% H_2/Ar).

reduction of Co_3O_4 to Co^0 occurs in a two-step process via the CoO intermediate.[34] The onset of Co_3O_4 conversion to Co^{2+} (first sharp peak) occurred at lower temperatures in the case of CTS catalyst (with the peak maximum at 181 °C) compared to the slightly higher temperature for CA (188 °C). The reduction to metallic Co (second broad feature) is also more facile for the CTS catalyst (occurring at about 226 °C) compared to the behavior of the CA catalyst (335 °C). This indicates that the Al_2O_3-based support hinders CoO reduction, compared to the titania-modified SiO_2 support, which has been reported[41,69,70] and was ascribed to differences in the interaction of Co_3O_4 particles with the supports. The peaks in the region between 600 and 1000 °C normally indicate the presence of metal−support composites.[68] In previously reported catalysts prepared on alumina, the amount of cobalt aluminate present in the calcined catalyst was usually small and difficult to detect with X-ray-based characterization methods,[71] but they are expected to be present at the interface.[72] In line with this, the TPR profiles indicate that there are likely small

https://doi.org/10.1021/acs.jpcc.5c05172
J. Phys. Chem. C XXXX, XXX, XXX−XXX

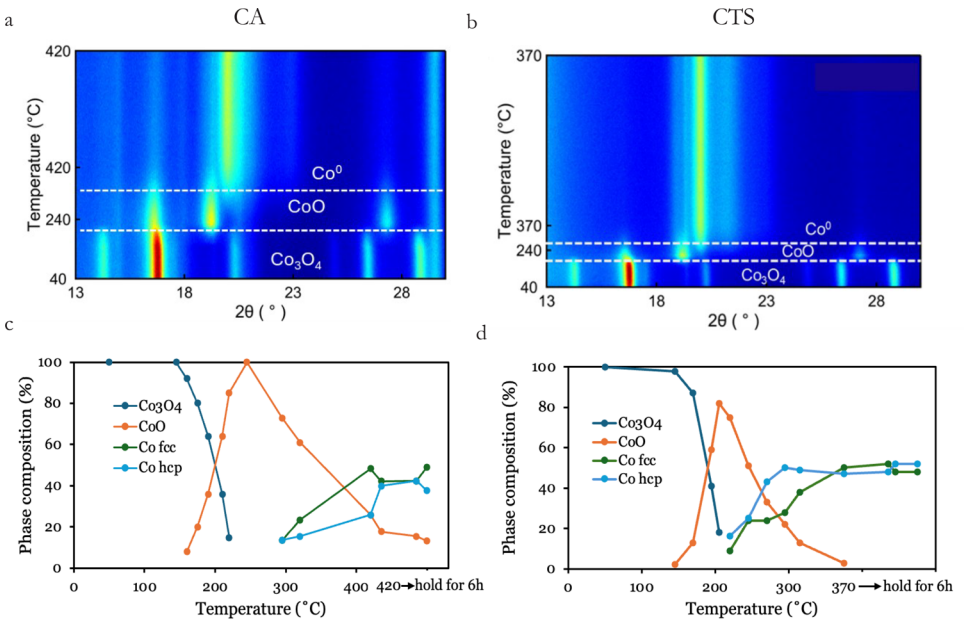

Figure 4. *In-situ* XRD during H_2 reduction (1 °C/min): 2D plot of the evolution of the XRD patterns (a, b) and the distribution of different Co phases (c, d) as a function of temperature and time on stream.

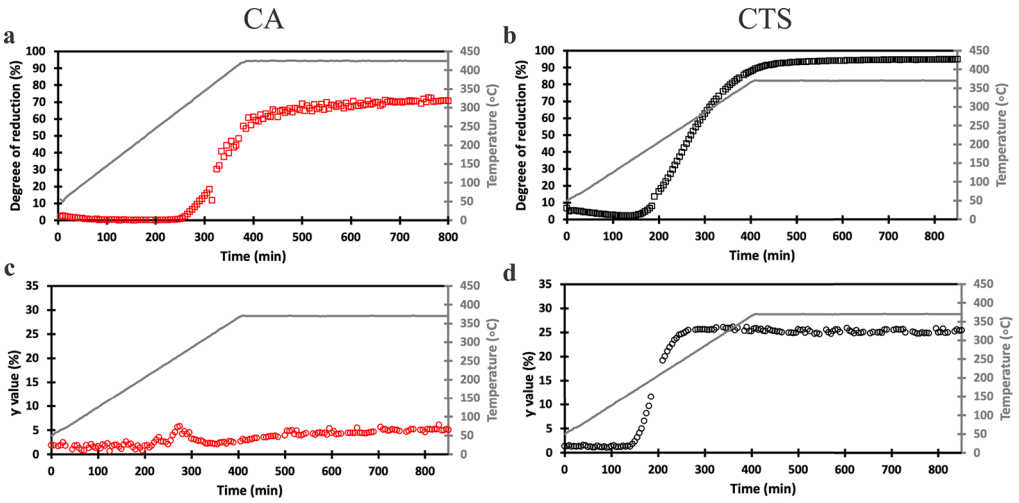

Figure 5. Reduction of the CA and CTS catalysts in H_2 monitored by *in-situ* magnetometry: the evolution of the degree of reduction of ferromagnetic Co (a, b) and of the γ value (c, d) with temperature and time on stream.

amounts of metal−support composites present in both systems, being more susceptible in the CA system. However, these may also form due to exposure to high temperatures during the TPR.

In-Situ Studies

In-situ XRD measurements during heating in pure H_2 (TPR, Figure 4, a−d) confirmed that both the CA and CTS catalysts are reduced to metallic Co in two steps via CoO as an intermediate phase, supporting the H_2-TPR results (Figure 3). The support once again influenced the onset temperature of reduction: the first reduction (Co_3O_4 to CoO) occurred at 240 °C and at 190 °C, while the second (CoO to Co^0) onset temperature was at 300 °C and at 260 °C for CA and CTS catalysts, respectively, in agreement with the H_2-TPR results. Moreover, the support influenced the degree of reduction, as indicated by the presence of the crystalline CoO phase in the CA and CTS catalysts (Figure 4, c and d, respectively). The average fcc/hcp ratios were 1.30 and 0.95 for CA and CTS, respectively. This indicates that the CTS support favors the formation or stabilization of hcp metallic cobalt. The crystallite sizes of Co_3O_4 were 21.5 and 20.0 nm for the CA and CTS catalysts, respectively. Upon Co_3O_4 reduction to CoO, the Co_3O_4 crystallite size decreased to 17 and 16 nm in CA and CTS, respectively. At the end of the reduction process, the CA catalyst consisted of CoO, fcc-Co^0, and hcp-Co^0 with Co crystallite sizes of 14, 6, and 6 nm, respectively, while in the CTS catalyst, only fcc-Co^0 and hcp-Co^0 were detected with crystallite sizes of 5 nm. The crystallite size of Co^0 was below 10 nm in the CA and CTS catalysts, indicating that during the reduction process, the Co_3O_4 particles shrank and broke up, resulting in smaller metallic Co crystallites. It is important to note that thermodynamically, the fcc allotrope is the stable allotrope below the size of 20 nm, while the hcp allotrope is stable above 20 nm.[73,74] Although both catalysts consisted of relatively high levels of the hcp phase, the crystallite size of

https://doi.org/10.1021/acs.jpcc.5c05172
J. Phys. Chem. C XXXX, XXX, XXX−XXX

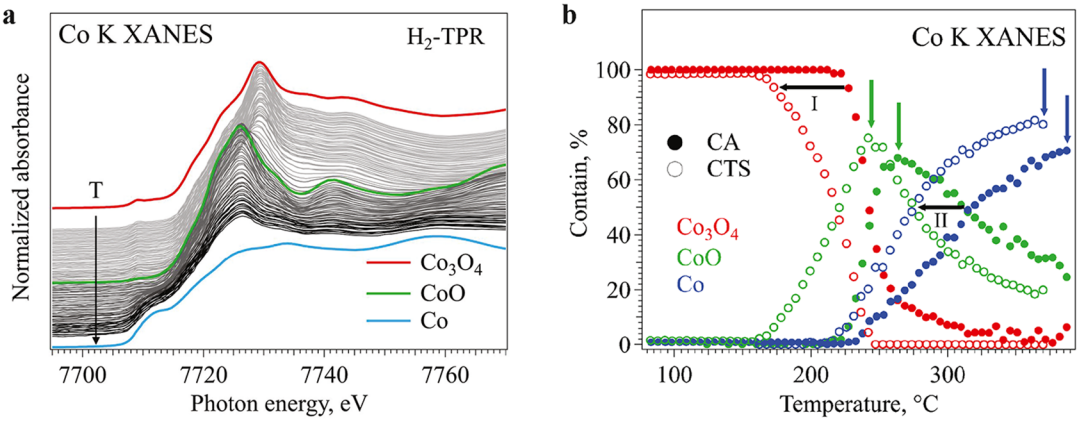

Figure 6. Evolution of the Co K XANES spectra of calcined CA catalyst during reduction in H_2 as a function of temperature (a) and the results of the linear combination analysis of the *in-situ* Co K XANES data for the CA (solid circles) and CTS (open circles) catalysts (b). The red, green, and blue curves/markers correspond to the data for Co_3O_4, CoO, and Co, respectively.

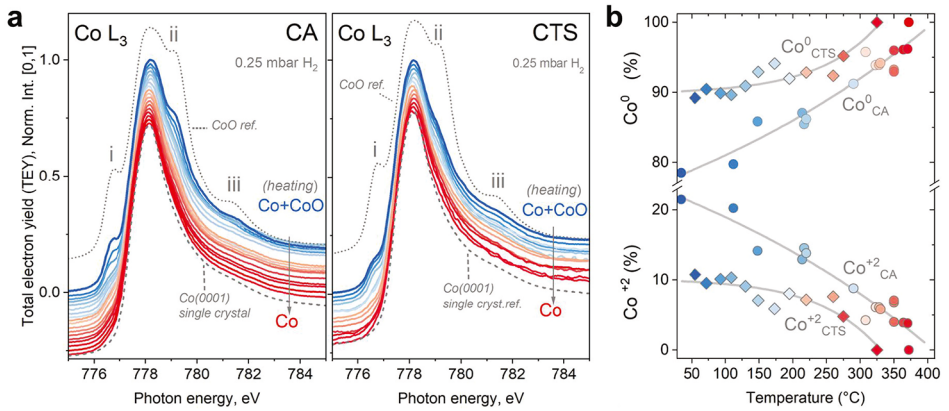

Figure 7. *In-situ* Co L_3-edge NEXAFS spectra of prereduced CA and CTS catalysts obtained in TEY mode during heating under 0.25 mbar of H_2. (a) Results of the linear combination analysis as a function of temperature: assuming a thermally activated process, the evolution of the quantified compositions was fitted with exponential functions. (b) More details are provided in SI, Section S2.

hcp-Co^0 is below 7 nm. This could be due to the intergrowth of the two phases (i.e., fcc and hcp), stabilizing the hcp allotrope with a crystallite size below 20 nm.[75−78] The smaller size of the Co_3O_4 crystallites in the calcined CA catalyst, which is thermodynamically harder to reduce, may further contribute to the observed lower reducibility.

The degree of reduction of Co_3O_4 to Co^0 in the CA and CTS catalysts was monitored using *in-situ* magnetometry (Figure 5). The onset of Co^0 formation (the ferromagnetic phase only) was at 250 °C and 185 °C for the CA and CTS catalysts, respectively, which is lower than that in the *in-situ* XRD reduction study (Figure 4) due to the higher sensitivity of magnetometry to small crystallites compared to XRD. The degree of reduction (DoR) of the CA and CTS catalysts reached a maximum of 71% and 95%, respectively. No phase other than the metallic Co phase was observed in the XRD patterns. Both the higher onset reduction temperature and lower DoR in CA catalysts compared to the CTS catalysts underline the stronger interaction between the Co_3O_4 crystallites and the Al_2O_3-based support compared to the silica-based one. Upon the formation of the Co^0 phase, the γ values were recorded to be 5 and 25 % for the CA and CTS catalysts, respectively, and remained constant during the 6 h holding step at the maximum temperature, indicating no sintering during the reduction of Co_3O_4 to Co^0, regardless of the support nature. The smaller γ value for the CA catalyst compared to the CTS is indicative of smaller crystallites and/or a lower fraction of the hcp-cobalt allotrope, which is in line with the crystallite size estimated by XRD.[77]

XAS measurements at the Co K edge were performed to unravel the reduction of both the amorphous and crystalline cobalt phases during heating in a H_2 atmosphere. During the reduction process, pronounced changes in the shape of the Co K X-ray absorption near-edge structure (XANES) spectra were observed (Figure 6a): the initial spectral characteristics of $Co^{3+/2+}$ in Co_3O_4 oxide with the absorption edge at about 7717.5 eV and the white line at about 7729.3 eV transformed to the typical ones for octahedral Co^{2+} in CoO oxide with an absorption edge at about 7716.3 eV and the white line at about 7726.3 eV at temperatures above 220 °C. After that, the Co^{2+} was reduced to Co^0, resulting in a Co K XANES spectrum typical of metallic Co with an absorption edge at 7709.0 eV. The temperature at which Co_3O_4 started to reduce to Co^{2+} (marked with the black arrow I in Figure 6b) and at which about 50% of Co^{2+} reduced to Co^0 (marked with the black arrow II in Figure 6b) is about 50 °C and 30 °C lower for the CTS catalyst compared to the CA catalyst, respectively. The maximum amount of Co^{2+} (marked with green arrows in Figure 6b) and final reduction degree of Co^0 (marked with blue arrows in Figure 6b) are about 7 and 15% higher in the

https://doi.org/10.1021/acs.jpcc.5c05172
J. Phys. Chem. C XXXX, XXX, XXX−XXX

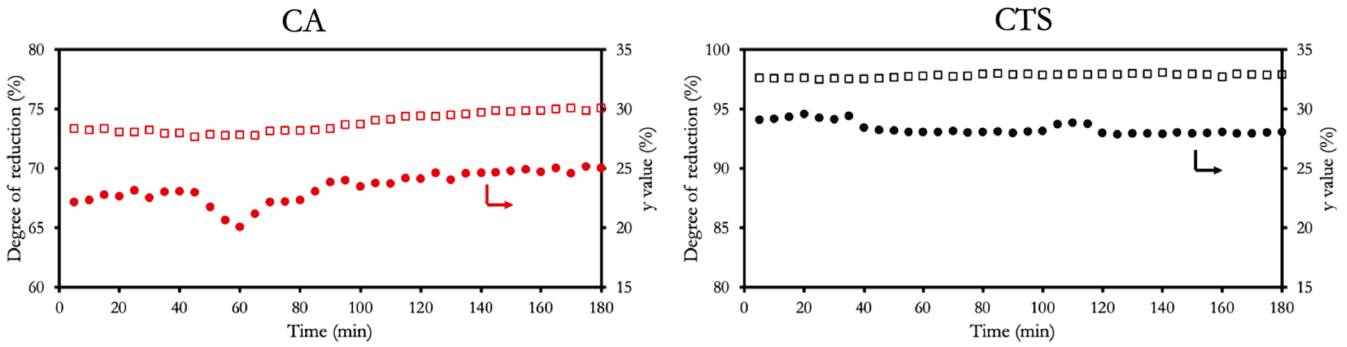

Figure 8. *Operando* magnetometry study under FTS conditions (T = 227 °C, p = 20 bar, H_2:CO = 2.0) to determine the effect of the support nature on the stability of CA (a) and CTS (b) catalysts: the degree of reduction (□) and of the γ value (°) with the time on stream.

CTS catalyst compared to those in CA, respectively. The results are in agreement with the H_2-TPR, *in-situ* XRD, and magnetometry results discussed above, but allow additional quantification of the Co^{2+} and Co^{3+} phases. Moreover, the XAS results showed that not all cobalt was reduced under the applied conditions.

The analysis of the shape of the Co K XANES spectra and the fitting of the Co K extended X-ray absorption fine-structure (EXAFS) data of the CA and CTS catalysts (cf. SI, Section S1) in the calcined and reduced state further revealed a slight deviation in the spectroscopic features from the spectra of the reference oxides for both materials, but with more pronounced deviations in the data of the CTS catalyst. This suggests the formation of a cobalt phase different from stoichiometric Co_3O_4 in the calcined state. In the reduced state, a higher degree of reduction is seen for the CTS catalyst. The similarity in the spectral shape of the CA catalyst to that of the CoO reference hints at the presence of unreduced Co in the Co^{2+} oxidation state.

Surface-sensitive *in-situ* near-edge X-ray absorption fine-structure (NEXAFS) spectroscopy at the Co L_3-edge of prereduced CA and CTS catalysts using total electron yield (TEY) was conducted, showing that Co was in principle completely reduced when approaching 325 and 375 °C, respectively (Figure 7). The initial state of the prereduced catalysts at low temperatures is a mixture of CoO and metallic Co. The presence of CoO is denoted by its spectral features (i), (ii), and (iii), which fade during heating under 0.25 bar of pure H_2 (Figure 7a). A comparison between the Co L_3 spectra at the maximum temperature (red curves) and the Co L_3 spectrum of a clean Co(0001) single crystal (gray dashed lines) indicates a practically complete reduction of cobalt in both catalysts. The linear combination analysis (Figure 7b) showed that initially, cobalt in the CTS catalyst was more reduced than that in CA, which completed the reduction at a higher temperature. As the probing depth in TEY mode for Co is about 2.5 nm,[79] which is significantly smaller than the Co crystallite size for these materials, as confirmed by XRD, it appears plausible to ascribe the unreduced Co present in Co^{2+} oxidation state, detected by the bulk sensitive XAS method (Figure 6), to mixed oxides at the metal−support interface that anchors the Co nanoparticles, but that the particles themselves are indeed metallic at the solid−gas interface.

EXAFS data after reduction were analyzed to uncover the local structure of cobalt (cf. additional information in the SI, Section S1). In the Fourier-transformed (FTF) Co K EXAFS data, no backscattering contributions corresponding to CoO (Co−O at 1.7 Å and Co−O−Co at 2.7 Å) were detected, which suggests the absence of a defined or long-range order in the CoO species remaining after the reduction of the CA catalyst. The intensity of the peak at 2.2 Å, corresponding to the first Co−Co coordination shell in metallic cobalt, allowed to estimate the size of the metallic particles: after reduction, the metallic cobalt particles are larger in the CTS catalyst compared to the metallic particles in the CA catalyst, as a higher amount of cobalt can be reduced in the CTS catalysts. Changes in the position and intensity of the peaks corresponding to the higher coordination shells of cobalt in the reduced catalysts compared to the reference cobalt are observed: peaks at 3.1 and 4.0 Å are shifted by 0.1 Å to lower values and the peak at 4.7 Å becomes less pronounced in the reduced catalysts, and the corresponding modification of the profile of the imaginary part of the Fourier transformed data between 2.5 and 3.0 Å is more pronounced in CA catalyst. A detailed analysis of the EXAFS data of Co foil at higher k values (Figure 12a) and fits to the hcp- and fcc-Co structures, on the one hand, demonstrates the challenge of fitting the bulk structure of cobalt with high precision, aiming to include coordination shells up to 6 and taking into account multiscattering effects. On the other hand, the experimental EXAFS data on the CA and CTS catalysts can be better fitted with the hcp structure than with fcc, although the number and position of the coordination shells do not differ significantly in these two phases, and mainly, multiscattering effects become visible in this case. Nevertheless, the significant contribution of the hcp-Co phase in the CA and CTS catalysts in the reduced state can be concluded, which is in agreement with the findings from *in-situ* XRD (see Figure 4). The changes observed in the EXAFS data of the CA and CTS catalysts (Figure 12b and c) can be attributed to the formation of fcc-domains after reduction and their preservation after cooling down to the room temperature, which may indicate an additional stabilizing role of the support for the fcc-domains of cobalt.[80] The effect is stronger in the CA catalyst compared to the CTS catalyst, similar to the findings from *in-situ* XRD.

Operando Studies

Operando magnetometry studies were performed for 2 h during the FTS, and Figure 8 shows the evolution of the DoR and γ values for the CA and CTS catalysts under industrially relevant conditions (T = 227 °C, p = 20 bar, H_2/CO = 2.0). Although the DoR and γ values remained constant for the CTS catalyst, a slight increase of the DoR (from 71 to 75%) and γ value (from 22 to 25%) was observed for the CA catalyst, indicating additional reduction under Fischer−Tropsch synthesis conditions, likely due to the presence of CO, which is a stronger

https://doi.org/10.1021/acs.jpcc.5c05172
J. Phys. Chem. C XXXX, XXX, XXX−XXX

reducing agent than H_2. In addition, some mild sintering has been reported previously.[49]

Operando magnetometry was employed for the determination of crystallite size distributions from magnetic measurements conducted after the reduction of the catalysts. This can be achieved by the application of the Langevin equation to the magnetic measurements, when the material displays superparamagnetic behavior (experimentally valid when $\gamma < 10\%$[29,50,52]). The results of the reduction studies show γ values of 5% and 25% for the CA and CTS catalysts, respectively, at 370° (see Figure 5). The temperature dependency of γ[53] can be utilized by conducting magnetic measurements at higher temperatures, resulting in lower γ values and the applicability of the Langevin equation. For the CTS catalyst, this novel approach was used to lower γ and enable magnetic-based particle sizing. The saturation magnetization and γ were recorded during this study at the measurement temperature and after cooling to 370 °C to ensure that no changes were induced in the catalyst during the measurement procedure. The effect of ramping temperature from 370 to 600 °C on the γ and magnetization of the samples can be seen in Figure 9, which shows a decrease in γ of about

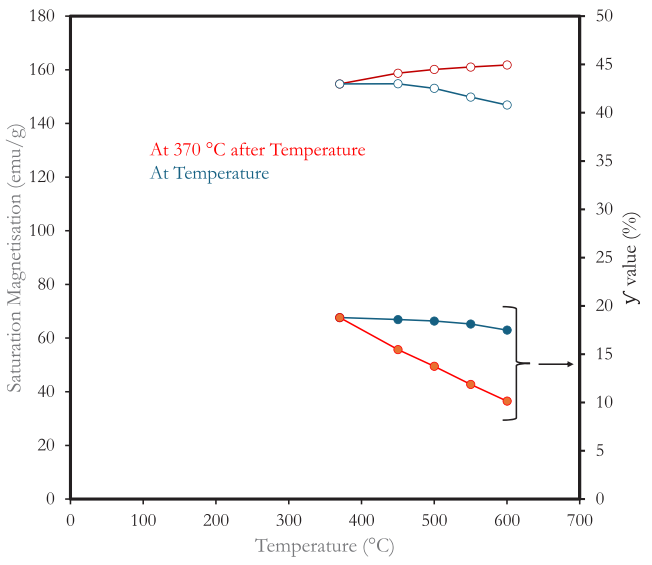

Figure 9. Effect of temperature on γ (a) and saturation magnetization (b) of CTS as a function of measurement temperature. The measurement procedure and temperature measurement points are described in the Methods section.

10% upon increasing the measurement temperature, thus enabling the magnetic measurements for crystallite size distribution determination. After returning to the reduction temperature (370 °C), there were small changes in both γ and saturation magnetization, indicating no significant changes in the catalyst during the measurement process. The crystallite size distributions are presented in Figure 10, and the average sizes are summarized in Table 2. The least-squares data provides marginally better fits to the data, with similar residual sums of squares obtained for both samples; however, the physical relevance of the log-normal fits makes these data a more likely representation of real catalysts. The average sizes obtained for the log-normal fits were 7.7 ± 2.9 nm and 9.2 ± 4.0 nm for the CA and CTS catalysts, respectively. It should be noted that the magnetic sizing will only include the reduced Co^0 material, and a lower degree of reduction for the catalyst CA will influence the magnetic sizing. These results provide a size measurement of the catalytically active phase, whereas other techniques, such as TEM, would present difficulties in distinguishing between metallic Co and unreduced cobalt oxides.

Operando Co K XAS measurements after 3 h under FTS conditions close to industrial relevance (T = 227 °C, p = 20 bar, H_2:CO = 2.0, identical to the magnetometry study) were conducted, revealing a different behavior of the Co particle CA and CTS catalysts (Figure 11). Cobalt continuously reduced further from 77% to 80% and 88% to 89% for CA and CTS, respectively. This was more pronounced for the CA catalyst, as seen in the modification of the XANES spectra toward metallic Co and an increase of the intensity of the Co−Co peaks at 2.2 Å in the Fourier-transformed EXAFS data. The amount of additionally Co reduced in the CA catalyst after the reaction was estimated to be about 3%, which is in agreement with the results of *operando* magnetometry. Note that only a low amount of material suitable for the transmission measurements can be loaded into the XAS microreactor; the reaction was performed under rather high space velocity conditions (63 N mL/gcat/s) and, as a consequence, a low conversion rate of CO (X_{CO} below 2%) and a low yield of gaseous CH_4 (X_{CH4} below 2%) for both the CA and CTS catalysts were achieved, confirmed by the activity tests in a small-scale reactor with a similar catalytic setup (3 N mL/gcat/s, X_{CO} ca. 30%, X_{CH4} ca. 12%).

Theoretical Considerations on Cobalt−Support Interactions

In order to shed light on the differences observed for CA and CTS catalysts, a series of density functional theory (DFT) calculations with respect to composite formation energies and adhesion of Co onto various oxide surfaces was performed. The formation energies of three composites, namely $CoTiO_3$, $CoAl_2O_4$, and Co_2SiO_4, were calculated (see Table 3). The formation of $CoAl_2O_4$ under FT reaction conditions (235 °C, 20 bar, and H_2:CO ratio of 2.0 at a CO conversion of 80%, thus having pH_2 = 2.0 bar and pH_2O = 5.3 bar, see SI, Section S3, Tables S1−S9 and Figure S2) is strongly exothermic with a formation energy of −26 kJ/mol, similar to the observations from earlier experimental[81] and theoretical[82] studies. This is in strong contrast to the formation of Co_2SiO_4, which is very endothermic (41 kJ/mol). The formation of cobalt titanite, envisioned to occur on the TiO_2-coated SiO_2 (and thus the CTS catalyst), is about thermoneutral under FT conditions (−2 kJ/mol). Although there is a strong driving force toward cobalt aluminate formation, this is basically absent for cobalt titanate, thus explaining the better reducibility and long-term stability of the CTS catalysts in comparison to CA. The adhesion energy of Co particles on various oxide and composite surfaces was further investigated (see results summarized in Table 3 and SI Section S3 for details about the calculations). As shown in Table 3, the adhesion on γ-Al_2O_3 and α-SiO_2 is rather small with values of −39.5 and −41.7 meV/Å^2, respectively, explaining the rapid sintering of Co on SiO_2 supports. Note that the formation of cobalt aluminate results in a higher adhesion energy of −76.3 meV/Å^2, thus preventing sintering to some degree, although at the expense of $CoAl_2O_4$ composite formation (see above). Interestingly, the adhesion of Co to TiO_2 surfaces (both anatase and rutile) is somewhat higher, being −45.6 (anatase) and −65.3 meV/Å^2 (rutile), while that on $CoTiO_3$ is as high as

https://doi.org/10.1021/acs.jpcc.5c05172
J. Phys. Chem. C XXXX, XXX, XXX−XXX

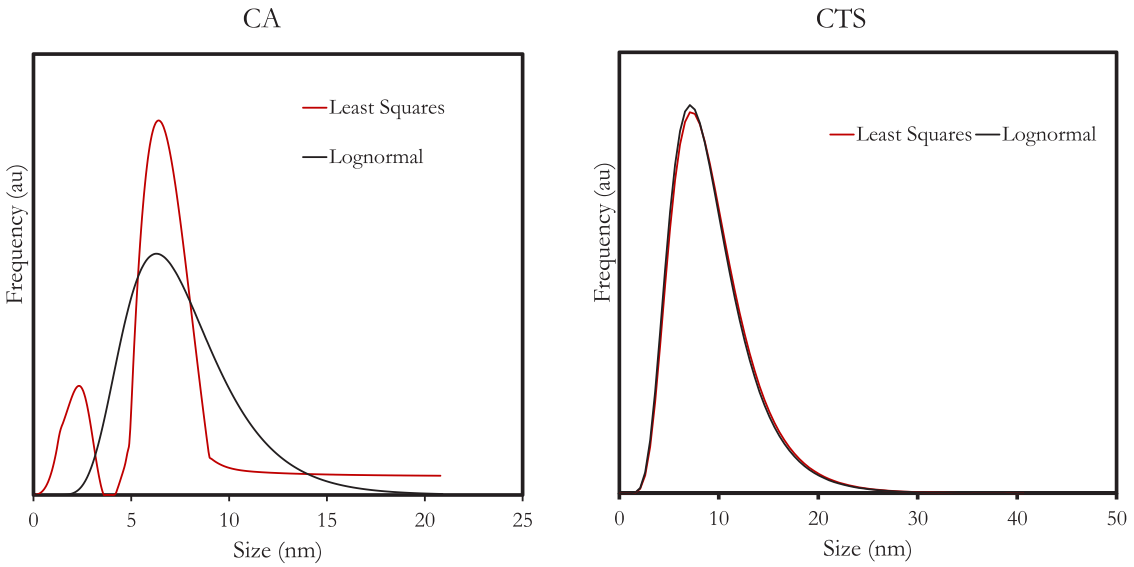

Figure 10. Crystallite size distribution of the CA and CTS catalysts determined by applying the Langevin equation to magnetic measurements.

Table 2. Summary of Average Crystallite Sizes Obtained from Magnetic-Based Crystallite Size Measurements for the CA and CTS Catalysts

	CA	CTS
Least-squares size (nm)	8.5 ± 5.7	9.9 ± 6.1
Log-normal Size (nm)	7.7 ± 2.9	9.2 ± 4.0

−101.7 meV/Å^2. The conclusion can be made that TiO_2-coated SiO_2 increases the adhesion of Co onto the oxide support while at the same time not being prone to composite formation to the extent observed for Al_2O_3. This increases the stability of Co/TiO_2−SiO_2 against sintering while at the same time preventing $CoTiO_3$ composite formation and thus the transformation of Co into an inactive phase, as evidenced by

Table 3. Calculated Composite Formation Energies (ΔG^f) under FTS Reaction Conditions (T = 235 °C, p = 20 bar, and H_2:CO = 2.0 at a CO Conversion of 80%; Thus, pH_2 = 2.0 bar and pH_2O = 5.3 bar) and Adhesion Energies Y_{adh} of Co on Various Oxide Surfaces

composite	ΔG^f, kJ/mol	Y_{adh}, meV/Å^2
TiO_2 (anatase)		−45
TiO_2 (rutile)		−64
$CoTiO_3$	−2	−103
γ-Al_2O_3		−39
$CoAl_2O_4$	−26	−76
α-SiO_2		−41
Co_2SiO_4	41	−66

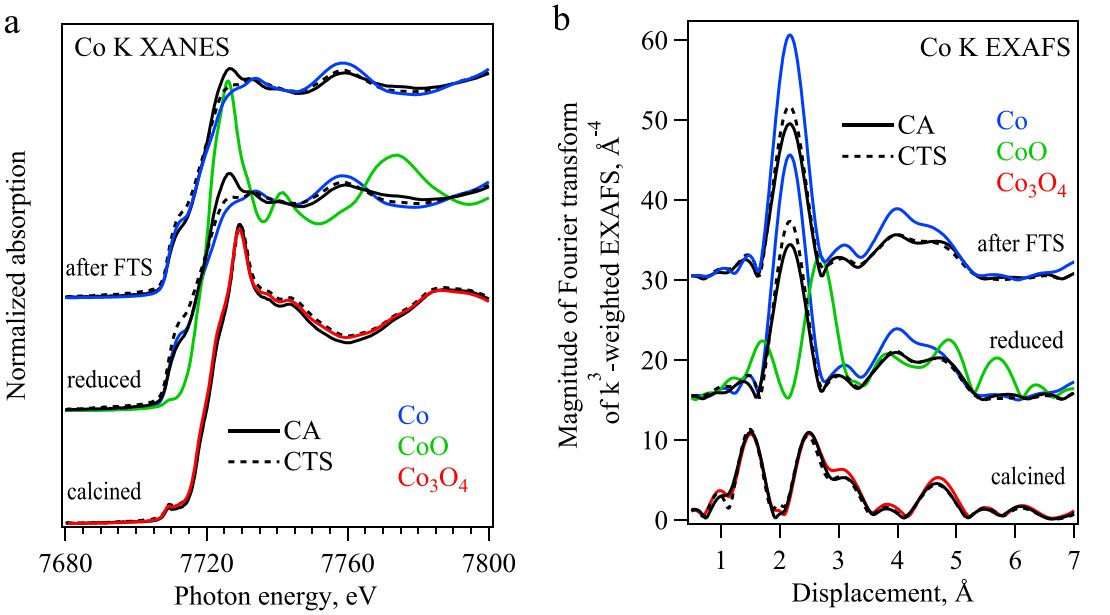

Figure 11. XANES spectra (a) and the corresponding k^3-weighted Fourier-transformed EXAFS data at the Co K-edge (not phase-corrected) (b) of CA and CTS catalysts in calcined and reduced states and after 3 h under FTS reaction conditions; the data of reference materials are shown for comparison.

https://doi.org/10.1021/acs.jpcc.5c05172
J. Phys. Chem. C XXXX, XXX, XXX−XXX

the higher degree of Co reduction as well as the higher stability during FT synthesis observed experimentally for the CTS catalyst compared to CA (Figure 8).

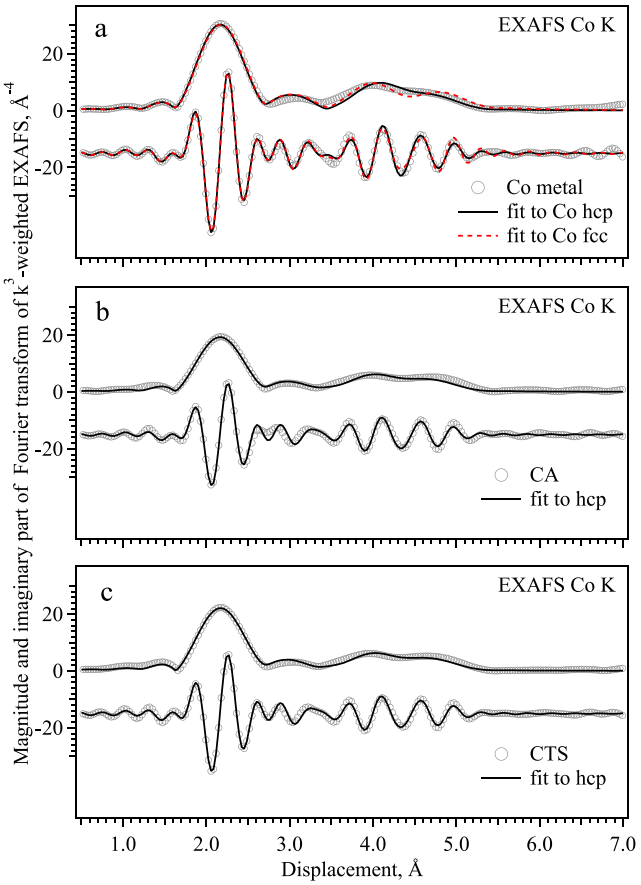

Figure 12. k^3-weighted Fourier-transformed EXAFS data at the Co K-edge (not phase-corrected) (marks) and fits (solid lines) to hcp-Co of (a) Co foil, (b) CA, and (c) CTS catalysts in the reduced state, the fit to fcc-Co (dashed line) of Co foil is shown for comparison.

The calculated Y_{adh} and Gibbs free energies (ΔG^f) thus suggest that Co binds to the support in the order TiO_2 > SiO_2 > γ-A_2O_3. Cobalt can be stabilized on alumina by the formation of $CoAl_2O_4$. Note that once Co reacts with the support, it is likely to remain in the Co^{2+} state. The calculations indicate that Co-support composite formation is more favorable in the order of $CoAl_2O_4$ > $CoTiO_3$ > Co_2SiO_4.

DISCUSSION

The study showed that the distinct differences in the activity, stability, and selectivity of the two selected industrial catalysts with a similar cobalt loading can probably be traced back to the morphology/porosity of the support grains and to the strength of the metal−support interaction, which defines the atomic structure of the active sites. For instance, although the sizes (Figure 8) of the cobalt oxide nanoparticles are similar in both catalysts, most of the Co is reduced in CTS, whereas about 20% of the cobalt remains oxidized in the case of the CA catalyst. The size of the metallic cobalt particles in the activated catalysts is still similar, below 10 nm (as observed by XAS, magnetometry, and XRD), which indicates a comparable dispersion of cobalt over both supports. The influence of Co nanoparticle size on catalytic activity is well established;[2] accordingly, magnetometry, XRD, and EXAFS analyses were employed to estimate the particle dimensions under *in-situ* conditions. Given the varying sensitivities of these techniques and the potential impact of support interactions on the cobalt particle size, these results highlight the complexity of accurately assessing this parameter. The identified differences in the reducibility of the two catalysts, which are directly related to their activity, can be mostly linked to the varying interactions with the two supports. Even though the initial crystallite sizes of Co_3O_4 differ, large sizes are expected to effectively suppress the effects of the structure-dependent reduction in H_2. Relatively small differences were previously observed for Co/Al_2O_3 model systems with Co_3O_4 sizes below 10 nm.[47] Further, when using graphitic carbon as a support with minimized interaction with Co_3O_4 nanoparticles, a mildly size-dependent reduction in H_2 was observed, which was most pronounced for small crystallite sizes below 6 nm.[83] The cobalt particle size in the catalysts studied in this work is within the range, where this value is supposed to influence the activity to a lesser extent.[2] The structural and performance parameters obtained by *in-situ*/*operando* H_2-TPR, NEXAFS, XRD, magnetometry (MM), and XAS on CA and CTS catalysts are summarized in Table 4.

The key factors defining the catalytic performance of Co-based catalysts are the textural properties of the support grains (for instance, pore size and tortuosity, defining the mass transportation of the reactants and products)[84,85] and the reducibility of the cobalt nanoparticles[21,22] related to their interaction with the support[12,20] during activation and under reaction conditions. An oxidic support with optimal porosity and a sufficient surface area can disperse cobalt particles well, but may affect their reducibility/stability if stable but nonactive species are formed on the support with a strong MSI. The CA catalyst has pores smaller than the average Co_3O_4 crystallite size, in contrast to the CTS catalyst, which might govern the catalytic performance of these two catalysts, as it defines the dispersion of cobalt over different supports and their mobility during the reaction. On supports with larger pores, which are less likely to suffer from diffusion limitations and allow better access to the active sites for reactants and easier transport of longer hydrocarbons, larger Co particles can form, which are easier to reduce. Supports with high pore volumes also allow higher Co loading with high dispersion (up to 30 wt.%) without the danger of agglomeration.

Various studies have reported that the degree of reduction of cobalt oxides on different oxidic supports decreases in the order γ-Al_2O_3 > TiO_2 > SiO_2.[33,70,86,87] In this work, larger portions of cobalt remained unreduced, and the reduction temperature of both reduction steps was higher for the CA catalyst than for the CTS catalyst, unraveled independently for different Co phases by *in-situ* XAS, XRD, and magnetometry. This suggests a stronger MSI for the CA catalyst than for the CTS. About 10−20% of cobalt remained unreduced, which might indicate the formation of an inactive solid-state phase between the cobalt and support, as the surface-sensitive NEXAFS in TEY mode studies ruled out the formation of an oxidic shell on the surface of the Co nanoparticles. The specification of the structure of the eventual solid phase is difficult, as it seems to be formed in minute quantities with short-range order and only after a long operation time.[88,89] The MSI between different supports and cobalt estimated in the present study is, at first glance, in disagreement with experimental observations that are generally reported. These

https://doi.org/10.1021/acs.jpcc.5c05172
J. Phys. Chem. C XXXX, XXX, XXX−XXX

Table 4. Comparison of Particle Size, Degree of Co Reduction, and Reduction Temperature for the Co/Al_2O_3 (CA) and $Co/TiO_2–SiO_2$ (CTS) Catalysts Obtained by Various Methods

		particle size, nm							
		Co_3O_4		Co^0		Co^0, %		T_{onset}, °C	
method	state	CA	CTS	CA	CTS	CA	CTS	CA	CTS
H_2-TPR	calcined							335	226
XRD	calcined	15.0	20.0	0	0	0	0		
in-situ XRD	calcined	21.5	20.0	0	0	0	0		
	activated	0	0	6.0	5.0	88	100	300	260
in-situ NEXAFS	calcined								
	activated					100[a]	100[a]	325[b]	375[b]
operando MM	activated			7.7	9.2	71	95	250	185
	spent					75	95		
operando XAS	calcined	>10	>10	0.0	0.0	0	0		
	activated	0.0[c]	0.0[c]	8.3[c]	9.3[c]	77	88	317[d]	276[d]
	spent	0.0[c]	0.0[c]	8.4[c]	9.2[c]	80	89		

[a]Surface sensitive. [b]Temperature extrapolated to 100% reduced state. [c]Co–Co 1st shell coordination number, ±0.2; S_0^2 = 0.70; Debye–Waller factor = 0.0065. [d]50% of Co is present in the Co^0 state.

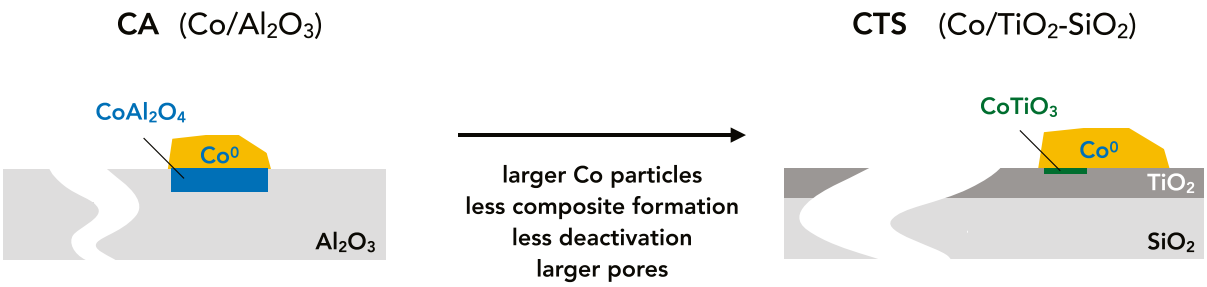

Figure 13. Schematic representation of the structures of the CA and CTS catalysts developed based on the results of the combined studies.

empirical findings can be explained by considering that Co interacts three times more strongly with Co-containing than with Co-free oxidic supports, as confirmed experimentally by data collected for liquid Co droplets by Campbell et al.[90,91] and summarized by Rahmati et al.[92]

The formation of $CoAl_2O_4$ over long FTS operation times has already been demonstrated[59] and is considered as one of the deactivation mechanisms for Co-based FT catalysts, although this solid-state reaction is characterized by relatively large energy barriers and the Gibbs free energy of formation of $CoAl_2O_4$ from Co^0 is negative under FTS conditions. $CoTiO_3$ and Co_2SiO_4 are unlikely to form during FTS because of their close to zero and positive ΔG^f values, respectively. The formation of the Co-support solid phase is more favorable from CoO at low operating temperatures, and the presence of H_2O during the FTS might further promote the MSI. Further long-term studies and theoretical considerations are necessary to elucidate these effects.

Based on the results reported here, combined characterization structural models for CA and CTS catalysts were developed, and the key parameters defining the activity/selectivity are depicted in Figure 13.

CONCLUSIONS

The higher CO conversion and higher selectivity toward C_{5+} for the silica-supported cobalt-based Fischer–Tropsch catalyst compared to the alumina-based catalyst can be traced back to the optimal porosity of the silica-based titania-modified support structure and weak cobalt–silica interaction, causing sufficient reduction and dispersion of the cobalt particles. The application of a combination of advanced characterization methods helped obtain a complete picture of the complex cobalt-support systems. One important aspect is the applicability of various characterization methods to trace specific parameters during the reaction process. Some of these methods are challenging to perform even under *in-situ* conditions, and certain information, like the formation of intermediates, might be difficult to quantify. Other methods provide information from the bulk of the material, not specifically probing the surface structure of the cobalt particles and supports, which are usually considered as active parts of powdered catalysts. Surface-sensitive methods, like NEXAFS, can provide complementary information. Imaging methods like X-ray tomography and its further developed synchrotron counterparts, including ptychography, can provide insights into the microstructure of the support at different stages of the reaction. By applying electron microscopy, high spatial resolution can be achieved, and the dynamics of the active

https://doi.org/10.1021/acs.jpcc.5c05172
J. Phys. Chem. C XXXX, XXX, XXX–XXX

sites and their interactions with the oxidic promoter can be studied in more detail.

An additional pathway to clarify the evolution of Co during FTS might be the characterization of model catalysts with simplified but industrially relevant structures. Attractive structure- and size-controlled synthesis methods include, for example, the surfactant-free benzyl alcohol route method[93] and flame spray pyrolysis.[94]

The use of the combined characterization approach introduced in this work will be beneficial to understand the evolution of cobalt and, in the future, the role and structure of, in most cases, oxidic promoters under industrially relevant operating conditions using challenging X-ray-based *operando* methods and to understand the stability and deactivation of catalysts over a long time scale.

■ ASSOCIATED CONTENT

Supporting Information

The Supporting Information is available free of charge at https://pubs.acs.org/doi/10.1021/acs.jpcc.5c05172.

Details of the EXAFS analysis, the linear combination analysis of NEXAFS data, and information on DFT calculations (PDF)

■ AUTHOR INFORMATION

Corresponding Authors

Anna Zimina − *Institute for Catalysis Research and Technology, Karlsruhe Institute of Technology, Eggenstein-Leopoldshafen 76344, Germany;* orcid.org/0000-0002-3111-7741; Email: anna.zimina@kit.edu

Jana Potgieter − *Sasol Research and Technology, Sasolburg 9570, South Africa*; Email: jana.taljaard@sasol.com

Catalina E. Jimenez − *Department Interface Design, Helmholtz-Zentrum Berlin für Materialien und Energie GmbH, Berlin 12489, Germany; Energy Materials In-Situ Laboratory Berlin, Helmholtz-Zentrum Berlin für Materialien und Energie GmbH, Berlin 12489, Germany;* orcid.org/0000-0002-8107-4399; Email: catalina.jimenez@helmholtz-berlin.de

Michael Claeys − *Catalysis Institute, Department of Chemical Engineering, University of Cape Town, Cape Town 7700, South Africa;* orcid.org/0000-0002-5797-5023; Email: michael.claeys@uct.ac.za

Authors

Mohamed I. Fadlalla − *Catalysis Institute, Department of Chemical Engineering, University of Cape Town, Cape Town 7700, South Africa*

Rabia Ilica − *Institute for Catalysis Research and Technology, Karlsruhe Institute of Technology, Eggenstein-Leopoldshafen 76344, Germany*

Enrico Sireci − *Institute for Catalysis Research and Technology, Karlsruhe Institute of Technology, Eggenstein-Leopoldshafen 76344, Germany*

Dmitry I. Sharapa − *Institute for Catalysis Research and Technology, Karlsruhe Institute of Technology, Eggenstein-Leopoldshafen 76344, Germany;* orcid.org/0000-0001-9510-9081

Dominic de Oliveira − *Catalysis Institute, Department of Chemical Engineering, University of Cape Town, Cape Town 7700, South Africa*

Cherie Hsu − *Institute for Catalysis Research and Technology, Karlsruhe Institute of Technology, Eggenstein-Leopoldshafen 76344, Germany*

Erisa Saraci − *Institute for Catalysis Research and Technology, Karlsruhe Institute of Technology, Eggenstein-Leopoldshafen 76344, Germany;* orcid.org/0000-0001-6770-5986

Moritz Wolf − *Institute for Catalysis Research and Technology, Karlsruhe Institute of Technology, Eggenstein-Leopoldshafen 76344, Germany;* orcid.org/0000-0002-1326-5337

Pinar Sakoglu − *Department Interface Design, Helmholtz-Zentrum Berlin für Materialien und Energie GmbH, Berlin 12489, Germany; Energy Materials In-Situ Laboratory Berlin, Helmholtz-Zentrum Berlin für Materialien und Energie GmbH, Berlin 12489, Germany*

Athanasios Skaltsogiannis − *Department Interface Design, Helmholtz-Zentrum Berlin für Materialien und Energie GmbH, Berlin 12489, Germany; Energy Materials In-Situ Laboratory Berlin, Helmholtz-Zentrum Berlin für Materialien und Energie GmbH, Berlin 12489, Germany*

Tianli Zhong − *Institute for Solar Fuels, Helmholtz-Zentrum Berlin für Materialien und Energie GmbH, Berlin 14109, Germany*

Marcus Bär − *Department Interface Design, Helmholtz-Zentrum Berlin für Materialien und Energie GmbH, Berlin 12489, Germany; Energy Materials In-Situ Laboratory Berlin, Helmholtz-Zentrum Berlin für Materialien und Energie GmbH, Berlin 12489, Germany; Friedrich-Alexander-University, Erlangen-Nürnberg 91054, Germany; Helmholtz Institute Erlangen-Nürnberg for Renewable Energy, Erlangen 91058, Germany;* orcid.org/0000-0001-8581-0691

Thys Botha − *Sasol Research and Technology, Sasolburg 9570, South Africa*

Denzil Moodley − *Sasol Research and Technology, Sasolburg 9570, South Africa*

Felix Studt − *Institute for Catalysis Research and Technology, Karlsruhe Institute of Technology, Eggenstein-Leopoldshafen 76344, Germany;* orcid.org/0000-0001-6841-4232

Jan-Dierk Grunwaldt − *Institute for Catalysis Research and Technology, Karlsruhe Institute of Technology, Eggenstein-Leopoldshafen 76344, Germany; Institute for Chemical Technology and Polymer Chemistry, Karlsruhe Institute of Technology, Karlsruhe 76131, Germany;* orcid.org/0000-0003-3606-0956

Complete contact information is available at: https://pubs.acs.org/10.1021/acs.jpcc.5c05172

Notes

The authors declare no competing financial interest.

■ ACKNOWLEDGMENTS

The authors gratefully acknowledge financial support of the German Federal Ministry of Research, Technology, and Space (BMFTR) within the CARE-O-SENE project (03SF0673). We would like to thank the Institute for Beam Physics and Technology (IBPT) for the operation of the storage ring and the Karlsruhe Research Accelerator (KARA). We acknowledge the KIT Light Source for providing instruments at the CAT-ACT beamline of the Institute of Catalysis Research and Technology (IKFT), particularly Dr. Danielle Santos Goncalves (IKFT) for her help and technical support during the

experiments. E.S., D.S., and F.S. acknowledge support from the state of Baden-Württemberg through bwHPC and the German Research Foundation (DFG) through grant no. INST 40/575-1 FUGG (JUSTUS 2 cluster, RVs bw17D011). Financial support from the Helmholtz Association, Germany, is gratefully acknowledged. The Energy Materials In-Situ Laboratory Berlin (EMIL) is acknowledged for providing the infrastructure to allow for sample preparation and X-ray analytics measurements. The support of Detre Trescher at the MPG-ISISS-beamline in BESSY II is gratefully acknowledged.

REFERENCES

(1) Moodley, D.; Botha, T.; Crous, R.; Potgieter, J.; Visagie, J.; Walmsley, R.; Dwyer, C. *Catalysis for a Sustainable Environment*; John Wiley & Sons, Ltd, Chapter 6, 2024; pp 73−116.
(2) Webb, P.; Filot, I. *Comprehensive Inorganic Chemistry lll*, 3rd ed.; Elsevier: Netherlands, 2023; pp 354−380.
(3) Kalz, K. F.; Kraehnert, R.; Dvoyashkin, M.; Dittmeyer, R.; Gläser, R.; Krewer, U.; Reuter, K.; Grunwaldt, J.-D. Future Challenges in Heterogeneous Catalysis: Understanding Catalysts under Dynamic Reaction Conditions. *ChemCatChem* **2017**, *9*, 17−29.
(4) Drünert, S.; Neuling, U.; Zitscher, T.; Kaltschmitt, M. Power-to-Liquid fuels for aviation: Processes, resources and supply potential under German conditions. *Appl. Energy* **2020**, *277*, No. 115578.
(5) Cabrera, E.; de Sousa, J. M. M. Use of Sustainable Fuels in Aviation − A Review. *Energies* **2022**, *15*, No. 2440, DOI: 10.3390/en15072440.
(6) Potgieter, J. H.; Moodley, D.; Botha, T.; Visagie, J.; Manong, T.; Frank, M.; Claeys, M.; van Steen, E.; Böltken, T.; Pfeifer, P. Development of promoted cobalt/alumina Fischer−Tropsch catalysts for increased activity and selectivity: Micro−reactor to piloting scale. *Catal. Today* **2024**, *432*, No. 114554.
(7) Voelker, S.; Groll, N.; Bachmann, M.; Mueller, L.; Neumann, M.; Kossioris, T.; Muthyala, P.; Lehrheuer, B.; Hofmeister, M.; Vorholt, A.; et al. Towards carbon−neutral and clean propulsion in heavy−duty transportation with hydroformylated Fischer−Tropsch fuels. *Nat. Energy* **2024**, *9*, 1220−1229.
(8) de la Peña O'Shea, V. A.; Consuelo Álvarez Galván, M.; Platero Prats, A. E.; Campos-Martin, J. M.; Fierro, J. L. G. Direct evidence of the SMSI decoration effect: the case of Co/TiO_2 catalyst. *Chem. Commun.* **2011**, *47*, 7131−7133.
(9) van Koppen, L. M.; Dugulan, A. I.; Hensen, E. J.; Bezemer, G. L. Tuning stability of titania−supported Fischer−Tropsch catalysts: Impact of surface area and noble metal promotion. *Catal. Today* **2024**, *429*, No. 114471.
(10) Du, H.; Jiang, M.; Zhao, M.; Ma, X.; Xu, Z.; Zhao, Z. Activity and selectivity enhancement of silica supported cobalt catalyst for alcohols production from syngas via Fischer−Tropsch synthesis. *Int. J. Hydrogen Energy* **2022**, *47*, 4559−4567.
(11) Khodakov, A. Y.; Bechara, R.; Griboval-Constant, A. Fischer−Tropsch synthesis over silica supported cobalt catalysts: mesoporous structure versus cobalt surface density. *Appl. Catal., A* **2003**, *254*, 273−288.
(12) Petersen, A. P.; Claeys, M.; Kooyman, P. J.; van Steen, E. Cobalt-Based Fischer−Tropsch Synthesis: A Kinetic Evaluation of Metal-Support Interactions Using an Inverse Model System. *Catalysts* **2019**, *9*, No. 794, DOI: 10.3390/catal9100794.
(13) Prieto, G.; De Mello, M. I. S.; Martínez, A.; Concepción, P.; Llorente, I. S.; Murciano, R.; Navarro, R. M.; Pergher, S. B. C.; Fierro, J. L. Cobalt-Catalyzed Fischer−Tropsch Synthesis: Chemical Nature of the Oxide Support as a Performance Descriptor. *ACS Catal.* **2015**, *5*, 3323−3335.
(14) Lin, T.; An, Y.; Yu, F.; Gong, K.; Yu, H.; Wang, C.; Sun, Y.; Zhong, L. Advances in Selectivity Control for Fischer−Tropsch Synthesis to Fuels and Chemicals with High Carbon Efficiency. *ACS Catal.* **2022**, *12*, 12092−12112.
(15) Johnson, G. R.; Werner, S.; Bell, A. T. An Investigation into the Effects of Mn Promotion on the Activity and Selectivity of Co/SiO2 for Fischer−Tropsch Synthesis: Evidence for Enhanced CO Adsorption and Dissociation. *ACS Catal.* **2015**, *5*, 5888−5903.
(16) Rommens, K. T.; Saeys, M. Molecular Views on Fischer−Tropsch Synthesis. *Chem. Rev.* **2023**, *123*, 5798−5858.
(17) Wolf, M.; Fischer, N.; Claeys, M. Capturing the interconnectivity of water-induced oxidation and sintering of cobalt nanoparticles during the Fischer−Tropsch synthesis in situ. *J. Catal.* **2019**, *374*, 199−207.
(18) Tsakoumis, N. E.; Walmsley, J. C.; Rønning, M.; van Beek, W.; Rytter, E.; Holmen, A. Evaluation of Reoxidation Thresholds for γ-Al_2O_3-Supported Cobalt Catalysts under Fischer−Tropsch Synthesis Conditions. *J. Am. Chem. Soc.* **2017**, *139*, 3706−3715.
(19) Moodley, D.; Saib, A.; van de Loosdrecht, J.; Welker-Nieuwoudt, C.; Sigwebela, B.; Niemantsverdriet, J. The impact of cobalt aluminate formation on the deactivation of cobalt-based Fischer−Tropsch synthesis catalysts. *Catal. Today* **2011**, *171*, 192−200.
(20) Wolf, M.; Fischer, N.; Claeys, M. Formation of metal-support compounds in cobalt−based Fischer−Tropsch synthesis: A review. *Chem. Catal* **2021**, *1*, 1014−1041.
(21) ten Have, I. C.; Weckhuysen, B. M. The active phase in cobalt−based Fischer−Tropsch synthesis. *Chem. Catal.* **2021**, *1*, 339−363.
(22) Claeys, M.; Dry, M. E.; van Steen, E.; van Berge, P. J.; Booyens, S.; Crous, R.; van Helden, P.; Labuschagne, J.; Moodley, D. J.; Saib, A. M. Impact of Process Conditions on the Sintering Behavior of an Alumina−Supported Cobalt Fischer−Tropsch Catalyst Studied with an in Situ Magnetometer. *ACS Catal.* **2015**, *5*, 841−852.
(23) Tucker, C. L.; van Steen, E. Activity and selectivity of a cobalt−based Fischer−Tropsch catalyst operating at high conversion for once−through biomass−to−liquid operation. *Catal. Today* **2020**, *342*, 115−123.
(24) Pestman, R.; Chen, W.; Hensen, E. J. Insight into the Rate-Determining Step and Active Sites in the Fischer−Tropsch Reaction over Cobalt Catalysts. *ACS Catal.* **2019**, *9*, 4189−4195.
(25) Hartman, T.; Geitenbeek, R.; Whiting, G.; Weckhuysen, B. M. Operando Monitoring of Temperature and Active Species at the Single Catalyst Particle Level. *Nat. Catal.* **2019**, *2*, 986−996.
(26) van Ravenhorst, I. K.; Hoffman, A. S.; Vogt, C.; Boubnov, A.; Patra, N.; Oord, R.; Akatay, C.; Meirer, F.; Bare, S. R.; Weckhuysen, B. M. On the Cobalt Carbide Formation in a Co/TiO_2 Fischer−Tropsch Synthesis Catalyst as Studied by High-Pressure, Long-Term Operando X-ray Absorption and Diffraction. *ACS Catal.* **2021**, *11*, 2956−2967.
(27) Yang, J.; Jacobs, G.; Jermwongratanachai, T.; Pendyala, V. R. R.; Ma, W.; Chen, D.; Holmen, A.; Davis, B. H. Fischer−Tropsch Synthesis: Impact of H_2 or CO Activation on Methane Selectivity. *Catal. Lett.* **2014**, *144* (1), 123−132.
(28) Fischer, N.; Clapham, B.; Feltes, T.; Claeys, M. Cobalt-Based Fischer−Tropsch Activity and Selectivity as a Function of Crystallite Size and Water Partial Pressure. *ACS Catal.* **2015**, *5*, 113−121.
(29) Wolf, M.; Kotzé, H.; Fischer, N.; Claeys, M. Size dependent stability of cobalt nanoparticles on silica under high conversion Fischer−Tropsch environment. *Faraday Discuss.* **2017**, *197*, 243−268.
(30) van Deelen, T. W.; Nijhuis, J. J.; Krans, N. A.; Zečević, J.; de Jong, K. P. Preparation of Cobalt Nanocrystals Supported on Metal Oxides To Study Particle Growth in Fischer−Tropsch Catalysts. *ACS Catal.* **2018**, *8*, 10581−10589.
(31) Eschemann, T. O.; Lamme, W. S.; Manchester, R. L.; Parmentier, T. E.; Cognigni, A.; Rønning, M.; de Jong, K. P. Effect of support surface treatment on the synthesis, structure, and performance of Co/CNT Fischer−Tropsch catalysts. *J. Catal.* **2015**, *328*, 130−138.
(32) Fratalocchi, L.; Visconti, C. G.; Lietti, L.; Groppi, G.; Tronconi, E.; Roccaro, E.; Zennaro, R. On the performance of a Co-based catalyst supported on modified γ-Al_2O_3 during Fischer−Tropsch synthesis in the presence of co-fed water. *Catal. Sci. Technol.* **2016**, *6*, 6431−6440.

https://doi.org/10.1021/acs.jpcc.5c05172
J. Phys. Chem. C XXXX, XXX, XXX−XXX

(33) Storsater, S.; Tøtdal, B.; Walmsley, J.; Tanem, B. S.; Holmen, A. Characterization of alumina−, silica−, and titania−supported cobalt Fischer−Tropsch catalysts. *J. Catal.* **2005**, *236*, 139−152.
(34) Jacobs, G.; Ji, Y.; Davis, B. H.; Cronauer, D.; Kropf, A. J.; Marshall, C. L. Fischer−Tropsch synthesis: Temperature programmed EXAFS/XANES investigation of the influence of support type, cobalt loading, and noble metal promoter addition to the reduction behavior of cobalt oxide particles. *Appl. Catal., A* **2007**, *333*, 177−191.
(35) Fischer, N.; van Steen, E.; Claeys, M. Structure sensitivity of the Fischer−Tropsch activity and selectivity on alumina supported cobalt catalysts. *J. Catal.* **2013**, *299*, 67−80.
(36) van Steen, E.; Claeys, M.; Dry, M. E.; van de Loosdrecht, J.; Viljoen, E. L.; Visagie, J. L. Stability of Nanocrystals: Thermodynamic Analysis of Oxidation and Re-reduction of Cobalt in Water/Hydrogen Mixtures. *J. Phys. Chem. B* **2005**, *109*, 3575−3577.
(37) Fischer, N.; Clapham, B.; Feltes, T.; van Steen, E.; Claeys, M. Size−Dependent Phase Transformation of Catalytically Active Nanoparticles Captured In−Situ. *Angew. Chem., Int. Ed.* **2014**, *53*, 1342−1345.
(38) Khodakov, A. Y.; Chu, W.; Fongarland, P. Advances in the Development of Novel Cobalt Fischer−Tropsch Catalysts for Synthesis of Long−Chain Hydrocarbons and Clean Fuels. *Chem. Rev.* **2007**, *107*, 1692−1744.
(39) Nabaho, D.; Niemantsverdriet, J. H.; Claeys, M.; van Steen, E. Hydrogen spillover in the Fischer−Tropsch synthesis: An analysis of gold as a promoter for cobalt−alumina catalysts. *Catal. Today* **2016**, *275*, 27−34.
(40) Van Berge, P. J.; Van De Loosdrecht, J.; Visagie, J. L. Process for Producing Hydrocarbons with Cobalt Catalysts. Europe Patent EP1299503B1, 2007.
(41) Labuschagne, J.; Meyer, R.; Chonco, Z. H.; Botha, J. M.; Moodley, D. J. Application of water−tolerant Co/β−SiC catalysts in slurry phase Fischer−Tropsch synthesis. *Catal. Today* **2016**, *275*, 2−10.
(42) Botha, J. M.; Moodley, D. J.; Potgieter, J. H.; Van Rensburg, H.; van de Loosdrecht, J.; Moodley, P. (Cape Catalytix). Cobalt—Containing Catalyst Composition. US Patent US1,278,870 2022.
(43) Coelho, A. A. Indexing of powder diffraction patterns by iterative use of singular value decomposition. *J. Appl. Crystallogr.* **2003**, *36*, 86−95.
(44) Rietveld, H. M. A profile refinement method for nuclear and magnetic structures. *J. Appl. Crystallogr.* **1969**, *2*, 65−71.
(45) Van Berge, P.; Visagie, J.; Van de Loosdrecht, J.; Van der Walt, T.; Sollie, J.; Sollie-Breur, S.; Veltman, H. Sasol Technology (Proprietary) Limited). Process for Activating Cobalt Catalysts. US Patent US7592289B2, 2009.
(46) Claeys, M. C. M.; Fischer, N. F. Cape Catalytix). Sample presentation device for radiation-based analytical equipment. US Patent US8,597,598B2, 2013.
(47) Fischer, N.; Claeys, M. Phase changes studied under in situ conditions — A novel cell. *Catal. Today* **2016**, *275*, 149−154.
(48) Claeys, M. C. M.; van Steen, E. W. J.; Visagie, J. L.; van de Loosdrecht, J. University of Cape Town). Magnetometer. US Patent US8.773.118B2, 2014.
(49) Claeys, M.; Dry, M.; van Steen, E.; du Plessis, E.; van Berge, P.; Saib, A.; Moodley, D. In−situ magnetometer study on the formation and stability of cobalt carbide in Fischer−Tropsch synthesis. *J. Catal.* **2014**, *318*, 193−202.
(50) Dalmon, J. *Catalyst Characterization: Physical Techniques for Solid Materials*; Springer US: New York: US, 1994; pp 585−607.
(51) Maphutha, M.; de Oliveira, D.; Nyathi, T. M.; Fadlalla, M. I.; Henkel, R.; Fischer, N.; Claeys, M. Hydrothermal Sintering and Oxidation of an Alumina-Supported Nickel Methanation Catalyst Studied Using In Situ Magnetometry. *Catalysts* **2021**, *11*, No. 636, DOI: 10.3390/catal11050636.
(52) Maphutha, M. In-Situ Sintering Study of Model Nickel Catalysts. PhD Thesis University of Cape Town: 2014.
(53) Moodley, D.; Claeys, M.; van Steen, E.; van Helden, P.; Kistamurthy, D.; Weststrate, K.-J.; Niemantsverdriet, H.; Saib, A.; Erasmus, W.; van de Loosdrecht, J. Sintering of cobalt during FTS: Insights from industrial and model systems. *Catal. Today* **2020**, *342*, 59−70.
(54) Kraft, D. *Forschungsbericht- Deutsche Forschungs- und Versuchsanstalt fur Luft- und Raumfahrt; A software package for sequential quadratic programming*, 1988.
(55) Virtanen, P.; Gommers, R.; Oliphant, T. E.; Haberland, M.; Reddy, T.; Cournapeau, D.; Burovski, E.; Peterson, P.; Weckesser, W.; Bright, J.; et al. Scipy 1.0: Fundamental Algorithms for Scientific Computing in Python. *Nat. Methods* **2020**, *17*, 261−272.
(56) Zimina, A.; Dardenne, K.; Denecke, M. A.; Doronkin, D. E.; Huttel, E.; Lichtenberg, H.; Mangold, S.; Pruessmann, T.; Rothe, J.; Spangenberg, T.; et al. CATACT − A new highly versatile X−ray spectroscopy beamline for catalysis and radionuclide science at the KIT synchrotron light facility ANKA. *Rev. Sci. Instrum.* **2017**, *88*, No. 113113.
(57) http://www.ibpt.kit.edu/KIT_Light_Source.php. accessed May 27, 2025.
(58) Newville, M. IFEFFIT: interactive XAFS analysis and FEFF fitting. *J. Synchrotron Radiat.* **2001**, *8*, 322−324.
(59) Loewert, M.; Serrer, M.-A.; Carambia, T.; Stehle, M.; Zimina, A.; Kalz, K. F.; Lichtenberg, H.; Saraçi, E.; Pfeifer, P.; Grunwaldt, J.-D. Bridging the gap between industry and synchrotron: an operando study at 30 bar over 300 h during Fischer−Tropsch synthesis. *React. Chem. Eng.* **2020**, *5*, 1071−1082.
(60) Haevecker, M. Innovative Station for In Situ Spectroscopy (ISISS). https://www.helmholtz-berlin.de/pubbin/igama_output?modus/einzel&sprache/en&gid/1671. accessed May 27, 2025.
(61) Kresse, G.; Furthmüller, J. Efficiency of ab-initio total energy calculations for metals and semiconductors using a plane-wave basis set. *Comput. Mater. Sci.* **1996**, *6*, 15−50.
(62) Kresse, G.; Hafner, J. Ab initio molecular dynamics for liquid metals. *Phys. Rev. B* **1993**, *47*, No. 558.
(63) Wellendorff, J.; Lundgaard, K. T.; Møgelhøj, A.; Petzold, V.; Landis, D. D.; Nørskov, J. K.; Bligaard, T.; Jacobsen, K. W. Density functionals for surface science: Exchange-correlation model development with Bayesian error estimation. *Phys. Rev. B* **2012**, *85*, No. 235149.
(64) Kresse, G.; Joubert, D. From ultrasoft pseudopotentials to the projector augmented-wave method. *Phys. Rev. B* **1999**, *59*, No. 1758.
(65) Liu, J.-X.; Su, H.-Y.; Sun, D.-P.; Zhang, B.-Y.; Li, W.-X. Crystallographic Dependence of CO Activation on Cobalt Catalysts: HCP versus FCC. *J. Am. Chem. Soc.* **2013**, *135*, 16284−16287.
(66) Liu, L.; Yu, M.; Wang, Q.; Hou, B.; Jia, L.; Chen, C.; Li, Z. Theoretically predicted surface morphology of FCC cobalt nanoparticles induced by Ru promoter. *Catal. Sci. Technol.* **2020**, *10*, 187−195.
(67) Dietze, E. M.; Plessow, P. N. Predicting the Strength of Metal−Support Interaction with Computational Descriptors for Adhesion Energies. *J. Phys. Chem. C* **2019**, *123*, 20443−20450.
(68) du Plessis, H. E.; Forbes, R. P.; Barnard, W.; Erasmus, W. J.; Steuwer, A. In situ reduction study of cobalt model Fischer−Tropsch synthesis catalysts. *Phys. Chem. Chem. Phys.* **2013**, *15*, 11640−11645.
(69) Nyathi, T. M.; Fadlalla, M. I.; Fischer, N.; York, A. P.; Olivier, E. J.; Gibson, E. K.; Wells, P. P.; Claeys, M. Support and gas environment effects on the preferential oxidation of carbon monoxide over Co3O4 catalysts studied in situ. *Appl. Catal., B* **2021**, *297*, No. 120450.
(70) Wolf, M.; Gibson, E. K.; Olivier, E. J.; Neethling, J. H.; Catlow, C. R. A.; Fischer, N.; Claeys, M. Water-Induced Formation of Cobalt-Support Compounds under Simulated High Conversion Fischer−Tropsch Environment. *ACS Catal.* **2019**, *9*, 4902−4918.
(71) Moodley, D.; Saib, A.; van de Loosdrecht, J.; Welker-Nieuwoudt, C.; Sigwebela, B.; Niemantsverdriet, J. The impact of cobalt aluminate formation on the deactivation of cobalt−based

https://doi.org/10.1021/acs.jpcc.5c05172
J. Phys. Chem. C XXXX, XXX, XXX−XXX

Fischer−Tropsch synthesis catalysts. *Catal. Today* **2011**, *171*, 192−200.
(72) Saib, A.; Borgna, A.; van de Loosdrecht, J.; van Berge, P.; Niemantsverdriet, J. XANES study of the susceptibility of nano−sized cobalt crystallites to oxidation during realistic Fischer−Tropsch synthesis. *Appl. Catal., A* **2006**, *312*, 12−19.
(73) Klugmann, E.; Blythe, H. J.; Walz, F. Investigation of thermomagnetic effects in monocrystalline cobalt near the martensitic phase transition. *Phys. Status Solidi A* **1994**, *146*, 803−813.
(74) Ram, S. Allotropic phase transformations in HCP, FCC and BCC metastable structures in Co-nanoparticles. *Mater. Sci. Eng A* **2001**, *304−306*, 923−927.
(75) Sławiński, W. A.; Zacharaki, E.; Fjellvåg, H.; Sjåstad, A. O. Structural Arrangement in Close-Packed Cobalt Polytypes. *Cryst. Growth Des.* **2018**, *18*, 2316−2325.
(76) Ducreux, O.; Rebours, B.; Lynch, J.; Roy-Auberger, M.; Bazin, D. Microstructure of Supported Cobalt Fischer−Tropsch Catalysts. *Oil Gas Sci. Technol. - Rev. IFP* **2009**, *64*, 49−62.
(77) du Plessis, H. E.; de Villiers, J. P. R.; Tuling, A.; Olivier, E. J. Stacking disorder in silicon carbide supported cobalt crystallites: an X-ray diffraction, electron diffraction and high resolution electron microscopy study. *Phys. Chem. Chem. Phys.* **2016**, *18*, 30183−30188.
(78) Price, S. W. T.; Martin, D. J.; Parsons, A. D.; Sławiński, W. A.; Vamvakeros, A.; Keylock, S. J.; Beale, A. M.; Mosselmans, J. F. W. Chemical imaging of Fischer−Tropsch catalysts under operating conditions. *Sci. Adv* **2017**, *3*, No. e1602838.
(79) Nakajima, R.; Stöhr, J.; Idzerda, Y. U. Electron-yield saturation effects in L-edge x-ray magnetic circular dichroism spectra of Fe, Co, and Ni. *Phys. Rev. B* **1999**, *59*, No. 6421.
(80) Sewak, R.; Dey, C. C.; Toprek, D. Temperature induced phase transformation in Co. *Nat. Sci. Rep.* **2022**, *12*, No. 10054.
(81) van Berge, P. J.; van de Loosdrecht, J.; Barradas, S.; van der Kraan, A. Oxidation of cobalt based Fischer−Tropsch catalysts as a deactivation mechanism. *Catal. Today* **2000**, *58*, 321−334.
(82) Wolf, M.; Fischer, N.; Claeys, M. Formation of metal-support compounds in cobalt-based Fischer−Tropsch synthesis: A review. *Chem. Catal.* **2021**, *1*, 1014−1041.
(83) Wolf, M.; Fischer, N.; Claeys, M. Preparation of isolated Co_3O_4 and fcc-Co crystallites in the nanometre range employing exfoliated graphite as novel support material. *Nanoscale Adv.* **2019**, *1*, 2910−2923.
(84) Moodley, D.; Botha, T.; Crous, R.; Potgieter, J.; Visagie, J.; Walmsley, R.; Dwyer, C. Catalysis for Sustainable Aviation Fuels: Focus on Fischer−Tropsch Catalysis. *Catal. Sustainable Environ. React.* **2024**, 73−166.
(85) Savostyanov, A. P.; Bakun, V. G. Relationship between the selectivity of the Fischer−Tropsch process and type of pore structure of cobalt catalysts. *Russ. J. Appl. Chem.* **2006**, *79*, 1839−1843.
(86) Jacobs, G.; Das, T. K.; Zhang, Y.; Li, J.; Racoillet, G.; Davis, B. H. Fischer−Tropsch synthesis: support, loading, and promoter effects on the reducibility of cobalt catalysts. *Appl. Catal., A* **2002**, *233*, 263−281.
(87) Riva, R.; Miessner, H.; Vitali, R.; Del Piero, G. Metal−support interaction in Co/SiO2 and Co/TiO2. *Appl. Catal., A* **2000**, *196*, 111−123.
(88) Saib, A.; Moodley, D.; Ciobîcă, I.; Hauman, M.; Sigwebela, B.; Weststrate, C.; Niemantsverdriet, J.; van de Loosdrecht, J. Fundamental understanding of deactivation and regeneration of cobalt Fischer−Tropsch synthesis catalysts. *Catal. Today* **2010**, *154*, 271−282.
(89) Moodley, D.; van de Loosdrecht, J.; Saib, A.; Overett, M.; Datye, A.; Niemantsverdriet, J. Carbon deposition as a deactivation mechanism of cobalt−based Fischer−Tropsch synthesis catalysts under realistic conditions. *Appl. Catal., A* **2009**, *354*, 102−110.
(90) Campbell, C. T. Ultrathin metal films and particles on oxide surfaces: structural, electronic and chemisorptive properties. *Surf. Sci. Rep.* **1997**, *27*, 1−111.
(91) Campbell, C. T.; Sellers, J. R. V. Anchored metal nanoparticles: Effects of support and size on their energy, sintering resistance and reactivity. *Faraday Discuss.* **2013**, *162*, 9−30.
(92) Rahmati, M.; Safdari, M.-S.; Fletcher, T. H.; Argyle, M. D.; Bartholomew, C. H. Chemical and Thermal Sintering of Supported Metals with Emphasis on Cobalt Catalysts During Fischer−Tropsch Synthesis. *Chem. Rev.* **2020**, *120*, 4455−4533.
(93) Wolf, M.; Fischer, N.; Claeys, M. Surfactant−free synthesis of monodisperse cobalt oxide nanoparticles of tunable size and oxidation state developed by factorial design. *Mater. Chem. Phys.* **2018**, *213*, 305−312.
(94) Teoh, W. Y.; Amal, R.; Mädler, L. Flame spray pyrolysis: An enabling technology for nanoparticles design and fabrication. *Nanoscale* **2010**, *2*, 1324−1347.

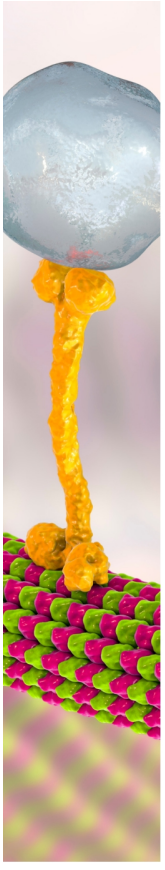

https://doi.org/10.1021/acs.jpcc.5c05172
J. Phys. Chem. C XXXX, XXX, XXX−XXX